Triple phase boundary specific pathway analysis for quantitative characterization of solid oxide cell electrode microstructure

Jørgensen, Peter Stanley; Ebbehøj, Søren Lyng; Hauch, Anne

Published in:
Journal of Power Sources

Link to article, DOI:
10.1016/j.jpowsour.2015.01.054

Publication date:
2015

Document Version
Peer reviewed version

Triple Phase Boundary Specific Pathway Analysis for Quantitative Characterization of Solid Oxide Cell Electrode Microstructure

P.S. Jørgensen[a,*], S. L. Ebbehøj[a] A. Hauch[a],

[a]Department of Energy Conversion and Storage, Technical University of Denmark, Risø Campus, Frederiksborgvej 399, 4000 Roskilde, Denmark.

* Corresponding author. E-mail: psjq@dtu.dk, Phone: +45 46775672.

S. L. Ebbehøj E-mail: slebb@dtu.dk

A. Hauch E-mail: hauc@dtu.dk

Abstract

The density and percolation of Triple Phase Boundary sites are important quantities in analyzing microstructures of solid oxide fuel cell electrodes from tomography data. However, these measures do not provide descriptions of the quality of the TPB sites in terms of the length and radius of the pathways through which they can be reached. New methods for performing TPB specific pathway analysis on 3D image data are introduced, analyzing the pathway properties of each TPB site in the electrode structure. The methods seek to provide additional information beyond whether the TPB sites are percolating or not by also analyzing the pathway length to the TPB sites and the bottleneck radius of the pathway. We show how these methods can be utilized in quantifying and relating the TPB specific results to cell test data of an electrode reduction protocol study for Ni/Scandia-and-Yttria-doped-Zirconia (Ni/ScYSZ) anodes. A study of the TPB density and particle size distribution alone did not provide an explanation for the differences observed in electrode performance. However, the analysis of pathway lengths to the TPBs and the bottleneck radii to reach these TPB sites provided valuable microstructural insight that supported the findings from the electrochemical characterization of the Ni/ScYSZ anodes.

Keywords: Triple phase boundary, Microstructure, Solid oxide cell, Characterization, 3D.

1. Introduction

In many electrochemical devices such as fuel cells, electrolysis cells and batteries the functionality is dependent on reactions occurring at specific sites with complex requirements. In the case of a Solid Oxide Fuel Cell (SOFC) anode, the electrode is typically a two phase porous structure. The triple phase boundaries (TPB) are the junctions between the two solid phases and the pore phase. At these sites ions can be conducted through the ion conducting phase, electrons can be conducted through the electron conducting phase and gas can reach and escape from the TPBs. For TPBs to be active, a percolating

pathway is required through each phase from the TPB to the respective sources or destinations (e.g. the electrolyte, gas supply and current collector).

Using techniques such as focused ion beam tomography [1-3] or X-ray tomography [4-6] a part of the 3D microstructure of an electrode can be digitally reconstructed for computational analysis. Much effort has been focused on quantifying both the density of the TPBs and whether those TPBs have percolating pathways to the relevant sources/destinations [7-11]. Considerable work has also been done in describing the internal structure of the networks of each phase to ultimately be able to predict the effective transport properties of each phase. The tortuosity of the phase network has been of particular interest [2,3,12] and the concept of constrictivity was recently re-introduced [13].

This work seeks to build on this prior work by combining the analysis of the TPBs with the analysis of the transport networks to be able to expand further on the quality of the TPB sites beyond being percolating or not. This is done by tying the properties of the transport network to the individual TPB sites. The work presented here can be seen as an extension of our previous work [14].

Holzer et al. [13] highlighted the difficulties in predicting transport properties from geometrical calculations on microstructures. Our focus on TPB specific transport properties takes a step further towards a functional analysis of the microstructure. However, the goals of the presented methods are not to predict the final transport properties, but instead seek to quantify properties that will assist in comparing, improving and understanding 3D electrode microstructures. Electrode microstructures are complex and challenging to assess manually and as will be shown below, important differences might be overlooked if only certain microstructural characteristics are considered.

The TPB specific pathway analysis is applied here to two SOFC Ni/ScYSZ anodes. The goal is to correlate differences in the electrochemical performance, as measured by impedance spectroscopy, to changes in the microstructure.

2. Experimental & Methodology

2.1. Cell specifications

The symmetric cells in this study were fully tape-cast cells from the same tape. They had 9 µm thick electrolytes of 10 mole percent scandia and 1 mole percent yttria stabilized zirconia (10Sc1YSZ) sandwiched between active NiO/10Sc1YSZ cermet anodes with thicknesses of ~40 µm. Mechanical support was obtained via ~330 µm thick anode support layers on each side made of porous NiO/3YSZ cermet. Further cell processing specifications have been reported elsewhere [15].

2.2. Test conditions and electrochemical characterization

Two different test startup procedures for the NiO reduction were applied to the symmetric cells to obtain the electro-catalytic porous Ni/10Sc1YSZ anodes. The details were reported previously [15]. The main differences in this reduction procedure for the two investigated symmetric cells were the temperature and gas composition during the NiO reduction. For the sample referred to as "HT-cell" (High Temperature cell), the cell was annealed and reduced at 1000 °C and during reduction, a gas stream of 3% H_2O in H_2 was applied. For the sample referred to as "LT-cell" (Low Temperature cell) the cell was annealed and reduced at 840 °C and during reduction dry H_2 was applied.

Electrochemical impedance spectroscopy (EIS) was used to characterize the electrochemical performance of the cells. The spectra were recorded in the frequency range from 1 MHz to 0.1 Hz. Further specifications for data recording and impedance data analysis are given in [15].

2.3. Image acquisition and processing

3D images of the two electrodes were acquired by focused ion beam tomography using a Zeiss XB1540 Crossbeam microscope. *Inlens* (positioned in the beam path) and *SE2* (Everhart-Thornley) detector images were acquired simultaneously at a voxel resolution of 24.4 x 24.4 x 41.9 nm. The two detector images were used to segment both data sets into the three phases: Pore, Ni and ScYSZ; using the method

described in [16]. A voxel cuboid of 364 x 505 x 228 voxels (8.9 x 12.3 x 9.6 µm) was extracted from both data sets, in a volume parallel to the electrolyte, with the z-axis (slicing direction) along the electrolyte. The volume begins approx. 2 µm from the electrolyte and extends into the active anode, but not into the support layer which has a significantly different microstructure. These two volumes of identical size and with the same relative location with respect to the electrolyte were used for all subsequent calculations and comparisons.

2.4. TPB density and continuous particle size distribution

TPB density and interface areas were calculated using the method described in [9]. The method described in [17] was used to calculate the continuous Particle Size Distributions (PSD).

2.5. TPB tortuosity

The TPB tortuosity is a measure of how twisted or tortuous the pathways are, which connect the individual TPB sites to their respective source or destination. The shortest distance from the TPB site to its source or destination is calculated, through a specific phase in the structure. This distance value is normalized by the direct distance to the TPB site across phase boundaries, thus giving rise to the tortuosity name. By performing the same calculation on every TPB site in the reconstructed microstructure (>1e5 sites in the present case) a distribution of the TPB tortuosity can be extracted. Note, that the TPB tortuosity is a purely geometrical measure with a simple definition that describes a characteristic of a single site in the microstructure. This TPB tortuosity should *not* be compared to the tortuosity factor, which is a considerably more complex characteristic of a network bulk property [13].

The calculation of TPB tortuosity is an extension of previous work described in [14]. The basis for the calculations is the ability to calculate the shortest distance between any two sets of voxels. To calculate the TPB tortuosity in a specific phase the voxels of that phase in the segmentation are assigned as *passable* and the voxels of all other phases are assigned as *blocked*. The first set of voxels (the *source*), for the distance calculation, are the voxels on one side of the voxel cuboid that are *passable*. The second

set of voxels (the *destination*), consists of all the TPB sites, which are voxels within the phase of interest that participate in a TPB. Figure 1 shows an illustration of the calculations on a 2D test structure in the black phase. Figure 1A shows the initial structure with the TPB sites circled. The *source* is the voxels within the black phase that are adjacent to the bottom edge (cuboid face in 3D). To calculate the TPB tortuosity, the distance from the *source* to every location within the black phase is calculated (see Figure 1B). The distance at the TPB sites is obtained by reading the value off the distance map at the TPB sites (the destination).

The TPB sites are identified during the TPB density calculation [9] as those voxels that share a TPB edge. Thus, a TPB site voxel is identified in each of the three phases for each TPB line segment. Using this setup the distance from one side of the voxel cuboid to all TPB sites in the microstructure is calculated in one pass. A similar calculation is performed with all voxels in the cuboid (all phases) assigned as *passable*, thus calculating the direct distance from each TPB site to the cuboid end face. The tortuosity at each TPB site is then obtained as the distance through the phase network divided by the direct distance. This calculation is performed for each of the three phases.

2.6. TPB critical pathway radius

This method calculates the radius of the thinnest section of the widest pathway that can be used to reach each TPB site in the structure. Alternatively it can be formulated as the radius of the largest sphere that can be passed through the network structure to a TPB site. The method is similar to the simulated mercury intrusion by Holzer et al. [13,18] but here the calculations are performed on a site specific basis. The foundation of the calculation is the pathway distance calculation used in the TPB tortuosity calculation above (Figure 1B). The strategy is to gradually shrink the network while keeping track of the percolation of each TPB site.

When applied initially, the pathway distance calculation will identify the percolating TPB sites as those with a measureable distance. If the network is eroded, by reducing the radius by the value r_{red}; pathways with an initial radius smaller than r_{red} will close. When the pathway distance calculations are performed again on the new structure, TPB sites that were initially dependent on those now closed pathways, will no longer be percolating. To identify the critical pathway radius of a specific TPB site, the pathway radius is reduced in small steps, each time checking the percolation of the TPB site. *The critical pathway radius is thus the r_{red} value where the TPB site first becomes non-percolating.* Figure 1C shows the reduction of the pathway radius to the point where a connection barely exists to three of the TPB sites. Figure 1E shows the situation where the same connection has just been lost.

By reducing the radius of the network pathways the TPB sites will no longer be part of the *passable* voxels for the distance calculation and it is thus not possible to read out their distance (the TPB sites are inside the grey area of Figure 1C&E). Since we are relying on the distance calculation to check for percolation an additional step is required in the calculation. A new distance map is calculated, this time with the percolating part of the eroded structure as the *source* (the black parts in Figure 1D&F) and the rest of the original structure set as *passable* (the black part of Figure 1A). This results in a distance map that can be evaluated at the TPB sites and holds the distance to the closest percolating part of the structure (the colored parts of Figure 1D&F). In this new distance map, a TPB site is considered percolating if its distance is less than r_{red}. By using the sphere analogy from before, it is not required that the center of the sphere can reach the TPB site, only that the surface of the sphere can reach it.

If the TPB site is in a concave region of the structure (the two lowest TPB sites on Figure 1D) they will be further away than r_{red}. The distance requirement is thus further relaxed to avoid measuring the local structure around the TPB site. In the sphere analogy this corresponds to just require that the surface of the sphere can reach within close proximity of the TPB site. For the 3D calculations presented below, a relaxation distance of 100 nm was used corresponding to approximately 2 voxel diagonals.

The length and radius characteristics of the pathways to the TPB sites are dependent on which starting plane is used as the source for the calculations. The analyses of TPB tortuosity and critical pathway radius are thus performed from all 6 sides of the voxel cuboids. This is done to assert the robustness of the calculations to variations in the microstructure close to the starting plane and to be able to detect possible anisotropy in the microstructure.

The pathway dependency of the calculations has the effect that TPB sites close to the source plane will have very low TPB tortuosity since a direct route is very likely to exist. Similarly, TPB sites close to the source plane are likely to have a larger critical pathway radius. To lessen this effect, only results from TPB sites further than 2.8 µm away from the source plane were included in the results. This value corresponds to twice the diameter of the largest particle size of any phase in the microstructures. Additionally, the exclusion of TPB sites close to the source reduces correlation between the results from opposite directions. The results presented below are based on the analysis of 145.000-195.000 TPB sites dependent on phase, direction and sample.

3. Results

3.1. Cell test results[1]

After the initial annealing of the cells and reduction of the NiO, the electrochemical performance of the cells was characterized by EIS. Table 1 gives a summary of the results from the electrochemical characterization of the HT-cell and LT-cell; reduced at 1000 °C and 840 °C, respectively. The impedance data was obtained at 750 °C with 40 % H_2O in H_2 led to the cells at 6 l/h. The equivalent circuit model developed by Ramos et al. was applied for Complex Non-linear Least Squares (CNLS) fitting of the

[1] The results from the electrochemical characterization of the cells analyzed via impedance spectroscopy were reported in detail previously [15]. A short summary is provided here for ease of comparison between obtained electrochemical performance and the results from the 3D reconstruction of the anode microstructures of the HT-cell and the LT-cell in this work.

impedance data [19]. From the work by Ebbehøj et al., summarized in Table 1, we observe the following: 1) The resistance attributed to the ionic resistance in the zirconia backbone of the electrodes (R_{ionic}) is identical for the two cells, indicating as expected that the zirconia backbone is not affected by the two different reduction profiles. 2) The resistance attributed to gas diffusion and conversion (R_{diff}) is slightly higher for the HT-cell compared to the LT-cell, indicating that the gas passage in the HT-cell might be more "hindered" in one way or another compared to the LT-cell. 3) The main difference in the polarization resistance of the cells is for the resistances attributed to the electrochemical reaction at the TPB (R_{TPB}). R_{TPB} is a factor of two higher for the LT-cell compared to the HT-cell, revealing that the LT-cell has fewer electrochemically active sites and/or that the individual sites are less active. 4) The Ohmic resistance (R_s) for the LT-cell is almost three times higher than for the HT-cell. The electrolyte is the same for the two cells and is expected not to be significantly affected by the two different start-up/reduction profiles. Thus, the difference in R_s can be ascribed to non-optimal Ni percolation and differences in the contacting of the cell in the test set-up. Low-voltage SEM images showing the percolating Ni network of the two cells (figure 4 in [15]) indicate poorer Ni percolation for the LT-cell. However, a factor of 3 in difference for R_s for cells having the same electrolyte strongly suggest that there is a difference in the contacting of the cells in the test set-up as well.

SEM micrographs (figure 3 in [15]) revealed qualitative differences in the electrode structures which can be summarized by: 1) For the HT-cell the Ni particles seemed better connected compared to the LT-cell and 2) For the LT-cell the porosities seemed to some extent to be distributed in-between the Ni particles and the ScYSZ backbone; a feature that was not observed in the HT-cell. Figure 2 provides a sketch of this observed difference in porosities around Ni particles for the two microstructures. For the HT-cell the Ni particles fill the "holes" in the zirconia backbone structure (Figure 2 HT), but in the LT-cell gaps (pores) appear on either side of the Ni particle and the TPBs are now located at the end of these thin cavities (Figure 2 LT).

3.2. Interfaces, TPB density and continuous PSD

Table 1 provides a summary of the results of the initial interface calculations on the two 3D microstructures from the two cells. Compared to the HT-cell, the LT-cell has a 26 % higher pore/ScYSZ interface area and a 35 % higher Pore/Ni interface area, at the cost of 25 % lower Ni/ScYSZ interface area. This supports the initial qualitative observations from SEM images in [15] that the low temperature reduction profile has caused pores to form between the Ni and ScYSZ phases (see Figure 2). The phase volume fractions show a small change in the pore/Ni ratio towards less Ni and more porosity in the low temperature sample. However, this is more likely to be due to variations in the microstructure or inaccuracies in the segmentation, than an actual bulk difference as the cells are cut from the same tape. No significant change is observed in the ScYSZ backbone in both the total ScYSZ interface area and the ScYSZ phase fraction.

The total TPB density is 13 % higher in the LT-cell compared to the HT-cell and the percolating TPB is 12 % higher. This is unexpected since the impedance data show that the resistance attributed to the electrochemical reactions at the TPB (R_{TPB}) is 103% larger in the LT-cell compared to the HT-cell.

Figure 3 shows the continuous (PSD) for all three phases for the two cells. As expected, the distributions show almost no difference for the ScYSZ backbone for the two cells. A shift towards smaller cavities in the pore phase is observed for the LT-cell. This is explained by the pore layers around the Ni phase (See Figure 2). The Ni PSDs are surprisingly similar for the two cells where the qualitative difference in structure does not translate into a significant difference in the PSDs. This absence of differences in the Ni PSD can be explained by the PSD calculation method. Consider the change in the Ni phase as two spheres that overlap for the HT-cell and two spheres (with similar diameter) that do not overlap for the LT-cell. The PSD calculation method essentially works by fitting overlapping spheres into the microstructure and as such will give almost the same result for those two microstructures.

3.3. TPB tortuosity

Figure 4 shows the reconstructed volume of the HT-cell and the LT-cell along with a plot of the shortest pathways for 300 randomly selected TPB sites through the Ni phase. The thickness of the lines is proportional to the number of pathways using it. Even before the assessment of the quantitative results the pathway plots show a clear difference in the pathway structure of the Ni network. The shortest pathways for the HT-cell can be seen to be almost parallel to the transport direction, and the pathways gather in many final pathways. The LT-cell pathways are considerably more tortuous and gather in fewer final pathways.

Figure 5 shows the TPB tortuosity for all three phases for both cells. Each curve is the average of the TPB tortuosity distribution obtained from performing the calculations in all 6 directions of the reconstructed microstructure. Figure 6 shows the cumulative distribution of the same data but with all 6 directions plotted for each sample. Note that the x-axes on the two plots are not the same.

Figure 5 shows a virtually identical TPB tortuosity distribution in the ScYSZ phase of the LT-cell and HT-cell, indicating that the network pathway structure of the ScYSZ phase does not change with the change in start-up procedures. Figure 6 shows that approx. 95 % of all the analyzed TPB sites in the ScYSZ phase have a TPB tortuosity lower than 1.2. This low TPB tortuosity is indicative of a structure with many alternative pathways to the TPB sites, thus ensuring that short pathways are very likely to exist.

A larger difference is observed in the pore phase between the LT-cell and the HT-cell in Figure 5 and Figure 6. The TPB sites of the LT-cell have less tortuous pathways than the HT-cell. Recall that the calculation method for TPB tortuosity does not depend on the pathway thickness but only on the length of the shortest possible direct pathway. The shift in TPB tortuosity in the pore phase between the two samples can thus be explained by the presence of the pores around the Ni in the LT-cell. The thin pore

cavities are likely providing additional short pathway options along the TPB curves in the pore cavities (LT image in Figure 2) thus making a short pathway more likely to exist.

A major difference is observed in the TPB tortuosity distributions of the Ni phases for the two cells; a difference which was not apparent from the continuous PSD of the Ni phases for the two cells. The difference is best observed in Figure 6. The LT-cell has a broad distribution of TPB tortuosity where a significant fraction of the TPB sites have TPB tortuosity in the range 2-4. Recall that this corresponds to the shortest possible pathway to the TPB site through the Ni phase being 2-4 times longer than the direct distance. The Ni phase network in the LT-cell thus consists of very tortuous and indirect pathways. From Figure 6 it is observed that approx. 95% percent of the TPB sites in the HT-cell have a Ni TPB tortuosity of 1.5 or less, while that only holds for 50-85 % of the TPB sites in the LT-cell. This large difference gives a measure of the difference in how "hindered" the access to the TPBs is through the Ni phase of the two microstructures.

3.4. TPB critical pathway radius

Figure 7 shows the results of the TPB critical pathway radius analysis. In the previously introduced sphere analogy, the plot shows how large a fraction of the TPB sites can be reached by a sphere of a certain radius (the critical pathway radius).

Almost identical distributions are seen in the ScYSZ phase between the two cells. This follows the previously seen trend of very insignificant changes in the ScYSZ network for the two cells.

For the LT-cell, the TPB sites in the pore phase are seen to be percolating through slightly narrower pore channels than for the HT-cell. Recall that the percolating TPB fraction at a critical pathway radius of zero corresponds to the conventional percolation check without the shrinkage of the network. The fraction of percolating TPBs in the LT-cell however drops more rapidly to zero than the HT-cell. This fits well with the TPB sites in the LT-cell being at the end of relatively narrow pores (see Figure 2).

The Ni phase shows a dramatic difference between the critical pathway radii of the two cells. For the LT-cell only 50% of the TPBs can be reached through a pathway with a radius larger than ~110 nm while 50% of the TPBs can be reached through a pathway with a radius larger than ~190 nm for the HT-cell. These results again highlights significant differences in the Ni network of the two cells; which were not revealed by the analyses of the continuous PSD and the TPB densities.

It is obvious that when fewer choices of pathways are available, a larger volume is needed to get robust results since the sampling statistics are worse. This is also what is observed; the curves for the 6 individual directions in the Ni phase are clustered much closer together in the HT-cell compared to the LT-cell (Figure 6) and almost no variation is seen in the ScYSZ phase.

4. Discussion

4.1. Electrode microstructures and their relation to electrochemical performance

The following hypothesis is based on the cell testing measurements and the TPB pathway analysis results: The differences in the connectivity of the Ni-Ni particles are the major causes of the performance differences between the two cells. While the Ni grains themselves do not change size considerably from the different reduction profiles (as seen from the PSDs), the number of alternative pathways between them and the cross-sectional area of the pathway bottlenecks are strongly affected by the differences in reduction protocols. The HT-cell has a well-connected structure with multiple pathways connecting each Ni phase junction; resulting in short pathway distances and thus low TPB tortuosity values. The LT-cell has a weakly connected Ni pathway structure, resulting in few alternative direct routes to the TPBs (Figure 4), thus increasing the pathway distance and the TPB tortuosity.

From the TPB pathway analysis it seems likely that the LT-cell has lost many of the Ni-Ni grain connections completely, indicated by the large increase in TPB tortuosity. Additionally, the Ni-Ni grain connections that are still intact suffer from narrow connections that create bottlenecks in the pathway

network. The bottlenecked TPBs in the LT-cell contribute to the percolating TPB density (Table 1) but the use of these TPB sites for electrochemical reactions will be accompanied by a higher resistance due to the increased pathway distance and the thinner pathway bottlenecks. Thus the TPB tortuosity and critical pathway thickness analyzed for these anode structures provide valuable supplementary information about the TPB sites and the pathways to reach these TPB sites, which in turn assist in interpretation of the observed differences in the electrochemical performance of the LT-cell and HT-cell (Table 1). It is important to note that the conductivity of Ni is high and it is unlikely that the increased resistance in the Ni network alone is the cause of the discrepancy in Ohmic resistance. However, it seems clear that the activity at the TPB sites will be reduced by the changes in the microstructure.

The investigated anodes were only used for initial electrochemical performance characterization and no long-term durability test was performed. However, the insight gained from the microstructural characterization presented here, provides valuable input for anode microstructure optimization for long-term durability. If we focus on the stability of the percolating Ni network we can state the following two characteristics based on the 3D data analysis: 1) The TPB critical pathway thickness (Figure 7) is significantly lower for the LT-cell than for the HT-cell; e.g. for 50% of the TPB sites to be reachable, spheres with a radius (pathway radius) smaller than ~110 nm is needed for the LT-cell but ~190 nm for the HT-cell. Therefore, the cross-sectional area of the narrowest Ni-Ni connection in the LT-cell is significantly smaller than in the HT-cell. This in turn means that in the LT-cell a disruption of a Ni-Ni connection is much more likely to occur, even though the PSDs are similar and would otherwise suggest equally robust networks. This could occur by nano-sized morphology changes by evaporation of smaller quantities of Ni (as nickel hydroxide e.g. during electrolysis testing), or by impurities building up at surfaces and interfaces. In other words, the Ni-Ni connections are vulnerable in a structure like the one observed in the LT-cell compared to the structure observed in the HT-cell. 2) Taking the results illustrated in Figure 4 as an example, it is also evident that in the structure of the LT-cell, many TPB sites use the same Ni-pathways i.e. in the LT-cell they gather in a few final pathways when compared to the HT-cell

structure. This means that a disruption of even a few Ni-Ni connections can have a significant detrimental effect on the pathway length and on the number of active TPB sites for the LT-cell compared to the HT-cell. In summary, the Ni-pathways are more vulnerable as disruption of a pathway is more likely to happen for the structure of the LT-cell compared to the HT-cell structure. Additionally, if/when such a disruption of a Ni-pathway occurs it is likely to be more detrimental to the LT-cell compared to the HT-cell. Such microstructure information is of high importance in the attempts to optimize the electrode structures for long-term durability.

4.2. Properties of the calculation methods

It is important to stress that the methods presented here calculate properties of the TPB sites and not of the network itself. This means that the TPB tortuosity does not directly relate to the tortuosity parameter often encountered in formulas for the effective transport properties [13] or even the geometrical tortuosity of the network itself [12]. The two calculated characteristics, TPB tortuosity and TPB critical pathway thickness are expected to be strongly correlated with the resistance in the network, but they do not give the complete picture. Aspects such as the amount of TPBs that are using the same pathways and the variation in thickness along the pathways [14] are not addressed. To take all aspects affecting the transport of ions, electrons and gas into account a finite element modeling approach should be pursued instead [20,21]. The presented characteristics are not meant to compete with a full functional modeling of the electrode but rather provide quantitative comparable microstructure characteristics that further describe the quality of the TPB sites beyond simply being percolating or not.

The fact that so similar results are obtained for each direction in Figure 6 and Figure 7 (except for the Ni network of the LT-cell) shows that a sufficiently large volume was used for the calculations. Even though the same volume is used for all 6 directions a different part of the volume is excluded for each direction (see section 2.6) and different pathways are used in each direction. The correlation between the 6 directions is thus reduced and the variation in the results from the 6 directions can be used to form a weak assessment of the uncertainty associated with the calculations. The similarity of the results in Figure 6 and

Figure 7 also shows that the calculated TPB characteristics are independent of direction and as such can be seen as bulk properties of the TPBs. However, the characteristics are still dependent on the size of the analyzed volume below a certain microstructure dependent size. Comparisons of structures should thus be made between volumes of comparable size whenever possible.

The computation time of the methods are taken up almost exclusively by the calculation of the distance maps [14]. Computation of the TPB tortuosity is relatively rapid, since only a single evaluation of the distance map is needed to compute the TPB tortuosity of all TPB sites. The critical pathway thickness takes considerably longer, since two new distance maps are calculated each time the phase network is eroded. The TPB tortuosity calculations presented here finishes in minutes on a single threaded implementation on an Intel(R) Xeon(R) W3550 CPU at 3.07GHz, whereas the TPB critical pathway thickness calculations take several hours to compute.

The methods presented here could easily be adapted to work with different materials, structures and devices. For instance in the case of electrodes utilizing phases of mixed ionic and electronic conduction (MIEC) the TPB sites could be exchanged for the sites adjacent to the MIEC/pore interface. It would thus be possible to obtain similar distributions of site specific tortuosity and critical pathway thicknesses for the active interface sites in such a structure.

5. Conclusion

Two new site specific parameters describing the quality of the TPBs were introduced. The TPB tortuosity, that seeks to quantify the distance from the TPB sites to the source/destination through each phase, and the TPB critical pathway thickness that seeks to quantify the bottleneck width of the pathways to the TPB sites.

The two methods were applied to analyze the differences in the microstructure of two Ni/ScYSZ based anodes, where two different reduction procedures were applied. The analysis showed a strong correlation

between the electrochemical performance test results and the differences in the microstructures of the two anodes, caused by the two different reduction procedures. Electrochemical performance tests showed that the cell reduced at low temperature (LT-cell) had a significantly higher resistance (especially the resistance assigned to the reactions at the TPB sites) compared to the cell reduced at high temperature (HT-cell). While the two cells surprisingly showed comparable TPB density and Ni phase PSDs, large differences were found in the quality of the TPB sites which was described and quantified in terms of TPB tortuosity and TPB critical pathway thickness. It was found and quantified that, in the Ni phase, the LT-cell had significantly longer (high TPB tortuosity) transport pathways, with narrower bottlenecks (small TPB critical pathway thicknesses) than the HT-cell.

Acknowledgements

The authors would like to thank colleagues at DTU Energy, especially Mogens B. Mogensen for valuable input and discussions and Tania Ramos for cell manufacturing as well as supervision, valuable input and discussions of the electrochemical studies of the cells. P. S. Jørgensen gratefully acknowledges financial support from the Programme Commission on Sustainable Energy and Environment, The Danish Council for Strategic Research, via the SERC project (www.serc.dk), contract no. 2104-06-0011.

References

[1] J.S. Cronin, K. Muangnapoh, Z. Patterson, K.J. Yakal-Kremski, V.P. Dravid, S.A. Barnett, J.Electrochem.Soc., 159 (2012) B385-B393.

[2] N. Vivet, S. Chupin, E. Estrade, A. Richard, S. Bonnamy, D. Rochais, E. Bruneton, J.Power Sources, 196 (2011) 9989-9997.

[3] D. Gostovic, J.R. Smith, D.P. Kundinger, K.S. Jones, E.D. Wachsman, Electrochem. Solid-State Lett., 10 (2007) B214-B217.

[4] Y. Karen Chen-Wiegart, J.S. Cronin, Q. Yuan, K.J. Yakal-Kremski, S.A. Barnett, J. Wang, J.Power Sources, 218 (2012) 348-351.

[5] P.R. Shearing, J. Gelb, J. Yi, W.K. Lee, M. Drakopolous, N.P. Brandon, Electrochem. Commun., 12 (2010) 1021-1024.

[6] G.J. Nelson, W.M. Harris, J.J. Lombardo, J.R. Izzo Jr., W.K.S. Chiu, P. Tanasini, M. Cantoni, J. Van herle, C. Comninellis, J.C. Andrews, Y. Liu, P. Pianetta, Y.S. Chu, Electrochem. Commun., 13 (2011) 586-589.

[7] Z. Jiao, N. Shikazono, N. Kasagi, J.Electrochem.Soc., 159 (2012) B285-B291.

[8] J.R. Wilson, W. Kobsiriphat, R. Mendoza, H. Chen, J.M. Hiller, D.J. Miller, K. Thornton, P.W. Voorhees, S.B. Adler, S.A. Barnett, Nat. Mater., 5 (2006) 541-544.

[9] P.S. Jørgensen, K.V. Hansen, R. Larsen, J.R. Bowen, J.Power Sources, 195 (2010) 8168-8176.

[10] P.S. Jørgensen, K. Yakal-Kremski, J. Wilson, J.R. Bowen, S. Barnett, J.Power Sources, 261 (2014) 198-205.

[11] H. Iwai, N. Shikazono, T. Matsui, H. Teshima, M. Kishimoto, R. Kishida, D. Hayashi, K. Matsuzaki, D. Kanno, M. Saito, H. Muroyama, K. Eguchi, N. Kasagi, H. Yoshida, J.Power Sources, 195 (2010) 955-961.

[12] Y.K. Chen-Wiegart, R. DeMike, C. Erdonmez, K. Thornton, S.A. Barnett, J. Wang, J.Power Sources, 249 (2014) 349-356.

[13] L. Holzer, D. Wiedenmann, B. Münch, L. Keller, M. Prestat, P. Gasser, I. Robertson, B. Grobéty, J.Mater.Sci., 48 (2013) 2934-2952.

[14] P.S. Jørgensen, K.V. Hansen, R. Larsen, J.R. Bowen, J.Microsc., 244 (2011) 45-58.

[15] S. Ebbehøj, T. Ramos, M. Mogensen, ECS Transactions, 45 (2012) 363-375.

[16] P.S. Jørgensen, K.V. Hansen, R. Larsen, J.R. Bowen, Ultramicroscopy, 110 (2010) 216-228.

[17] B. Munch, L. Holzer, J Am Ceram Soc, 91 (2008) 4059-4067.

[18] L. Holzer, B. Iwanschitz, T. Hocker, L. Keller, O. Pecho, G. Sartoris, P. Gasser, B. Muench, J.Power Sources, 242 (2013) 179-194.

[19] T. Ramos, J. Hjelm, M. Mogensen, J.Electrochem.Soc., 158 (2011) B814-B824.

[20] J. Joos, M. Ender, T. Carraro, A. Weber, E. Ivers-Tiffée, Electrochim.Acta, 82 (2012) 268-276.

[21] T. Carraro, J. Joos, B. Rüger, A. Weber, E. Ivers-Tiffée, Electrochim.Acta, 77 (2012) 315-323.

Table 1: Summary of results from electrochemical performance tests and basic microstructure characterization. All resistances are results reported by Ebbehøj et al. and based on CNLS fitting using an equivalent circuit model for analyzing the impedance data [15]. Impedance spectra were recorded at 750 °C with 40 % H_2O in H_2 led to the cells. The microstructure data was obtained by 3D reconstruction of each sample. The percolating TPB length calculations are averages of calculations performed in 6 directions with the ScYSZ phase percolation check being performed in the opposite direction of the pore and Ni phase percolation checks.

		HT-cell	LT-cell	Relative difference 100*(LT-HT)/HT [%]
Reduction conditions		3% H_2O in H_2, 1000 °C	Dry H_2, 840 °C	-
R_s	[mΩcm^2]	27	71	158
$R_{p,\,tot}$	[mΩcm^2]	77	120	56
R_{ionic}	[mΩcm^2]	14	13	-9
R_{TPB}	[mΩcm^2]	47	95	103
R_{diff}	[mΩcm^2]	16	12	-22
Total TPB_L	[µm/µm^3]	4.1	4.7	13
Percolating TPB_L	[µm/µm^3]	3.5	3.9	12
Pore/ScYSZ interface	[µm^2/µm^3]	1.2	1.6	26
Pore/Ni interface	[µm^2/µm^3]	0.9	1.2	35
Ni/ScYSZ interface	[µm^2/µm^3]	1.1	0.8	-25
Pore interface	[µm^2/µm^3]	2.2	2.8	30
ScYSZ interface	[µm^2/µm^3]	2.4	2.4	2
Ni interface	[µm^2/µm^3]	2.0	2.1	2
Pore volume fraction	[-]	0.29	0.31	8
ScYSZ volume fraction	[-]	0.36	0.37	2
Ni volume fraction	[-]	0.35	0.32	-8

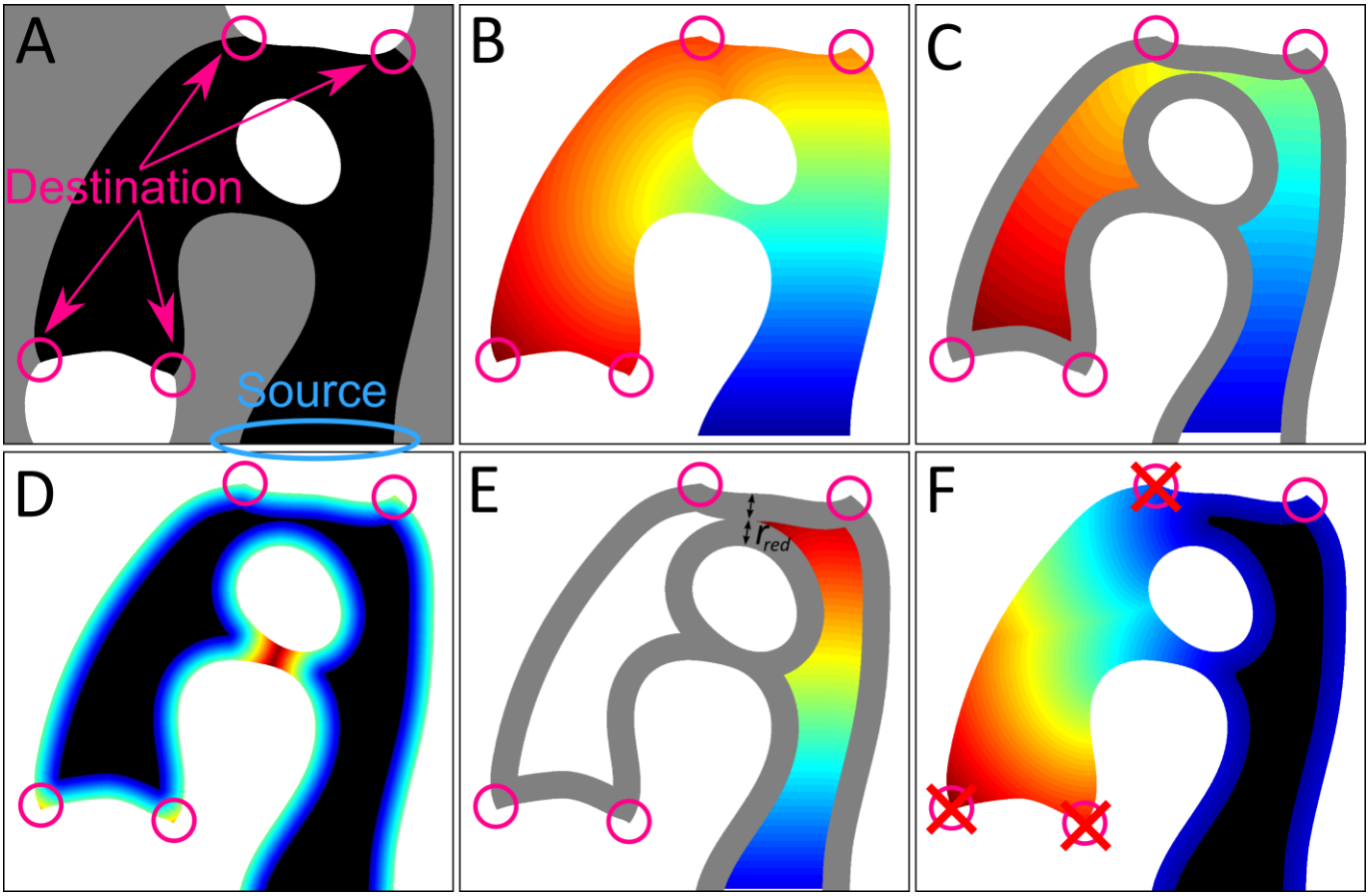

Figure 1: Illustration of the calculation of TPB tortuosity and TPB critical pathway radius. (A) An example 2D structure with 4 TPB sites (circled), the connectivity of the TPBs through the black phase to the edge of the structure is of interest. (B) Calculation of the distance from the edge of the structure to the TPB sites through the black phase in A. Distances are in arbitrary units with distance increasing from dark blue to red colors (black to white in printed version). (C) The boundaries of the black phase network in A have been eroded to the point where there is only a very narrow pathway to the two TPBs in the lower part of the structure. Grey indicates the part of the network that has been lost from the boundary erosion. (D) The TPB distance check for percolation based on the diameter reduction in C. The color coding indicates the distance from the percolating part of the structure in C. (E) The boundaries of the black phase network in A has been eroded to the point where there is no longer a connection to the two TPBs in the lower part of the structure. (F) The TPB distance check for percolation based on the boundary erosion in E. Three of the four TPB sites are not percolating at this erosion level because they are further than r_{red} away from the percolating structure in E.

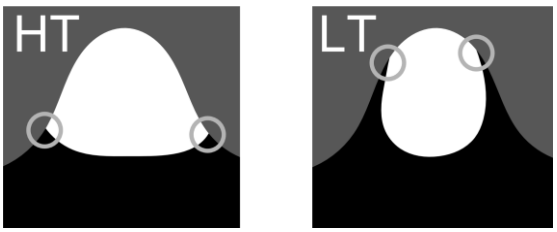

Figure 2: Sketch of the observed differences in the pore structure around the Ni in the HT-cell and the LT-cell. Black corresponds to pore, gray to ScYSZ and white to Ni. The light grey circles indicate the TPB sites.

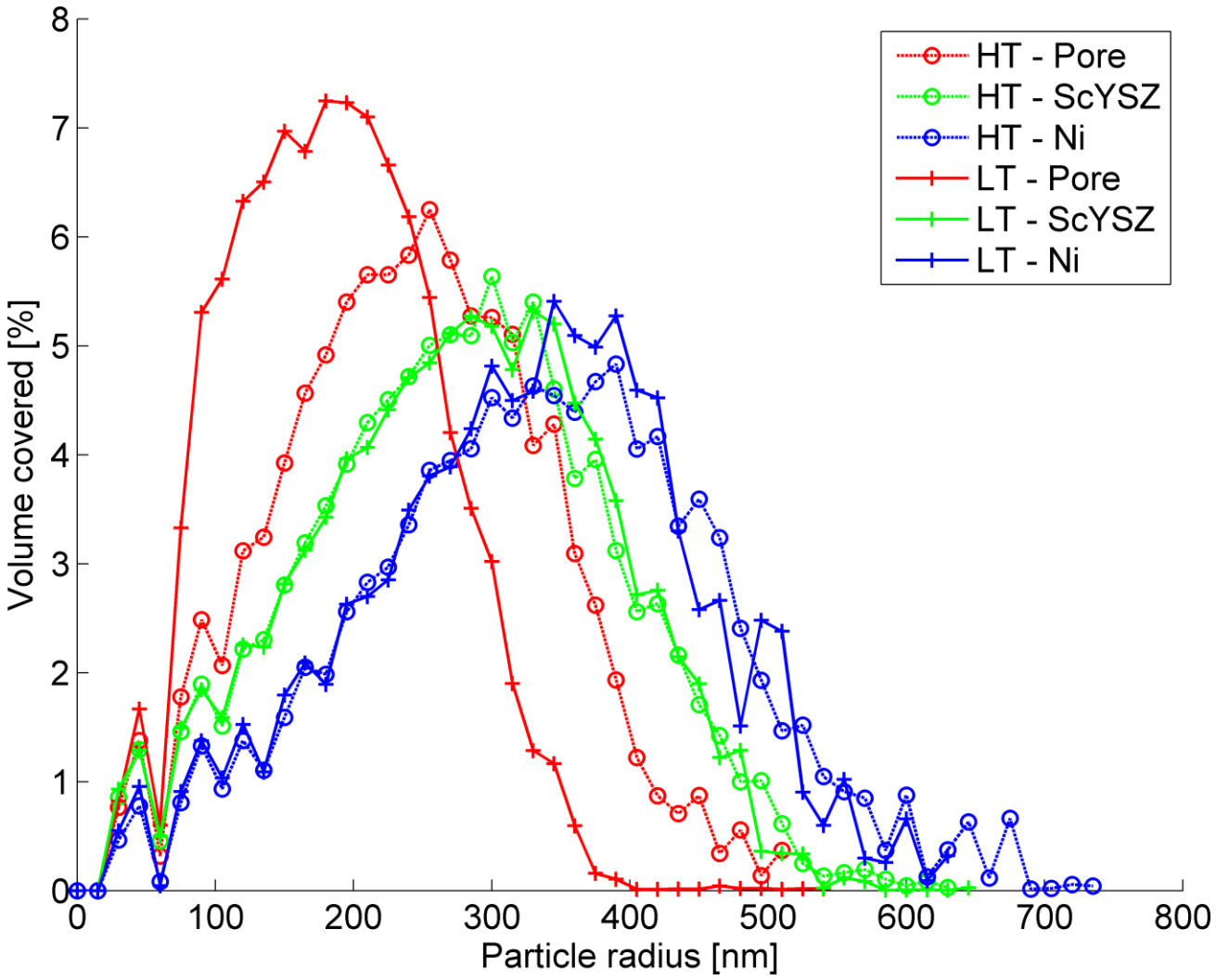

Figure 3: Continuous PSDs of the two cells including all three phases.

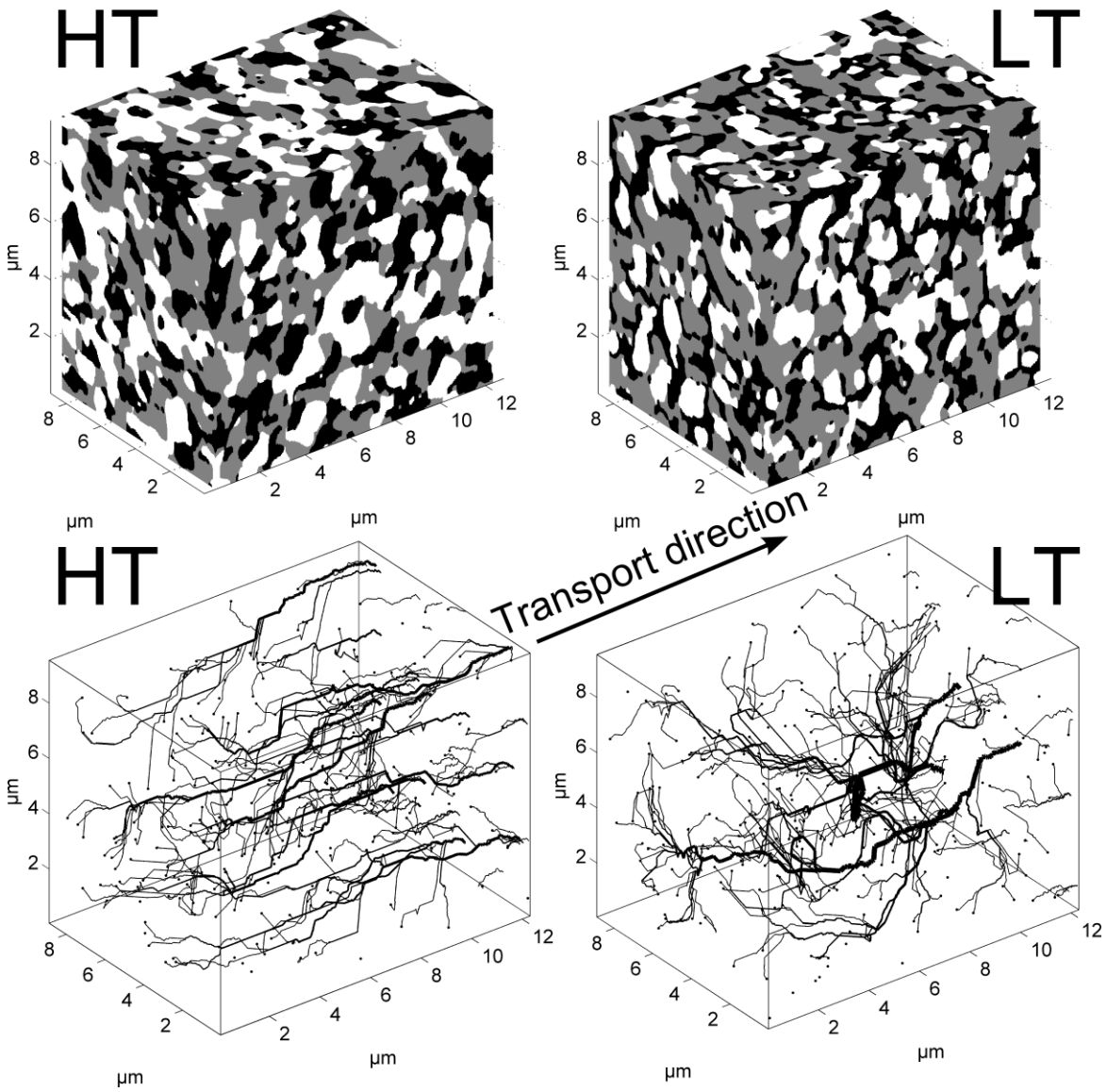

Figure 4: Segmented image data and TPB pathways in the Ni phase for the HT and LT-cells. (Top) The segmented 3D image data, black is pores, grey is ScYSZ and white is Ni. (Bottom) Pathways for 300 randomly selected TPB sites. The black lines show the shortest pathway from the TPB sites to the right most end plane through the Ni phase. The black dots are the TPB sites and the thickness of the lines is proportional to the number of pathways using it.

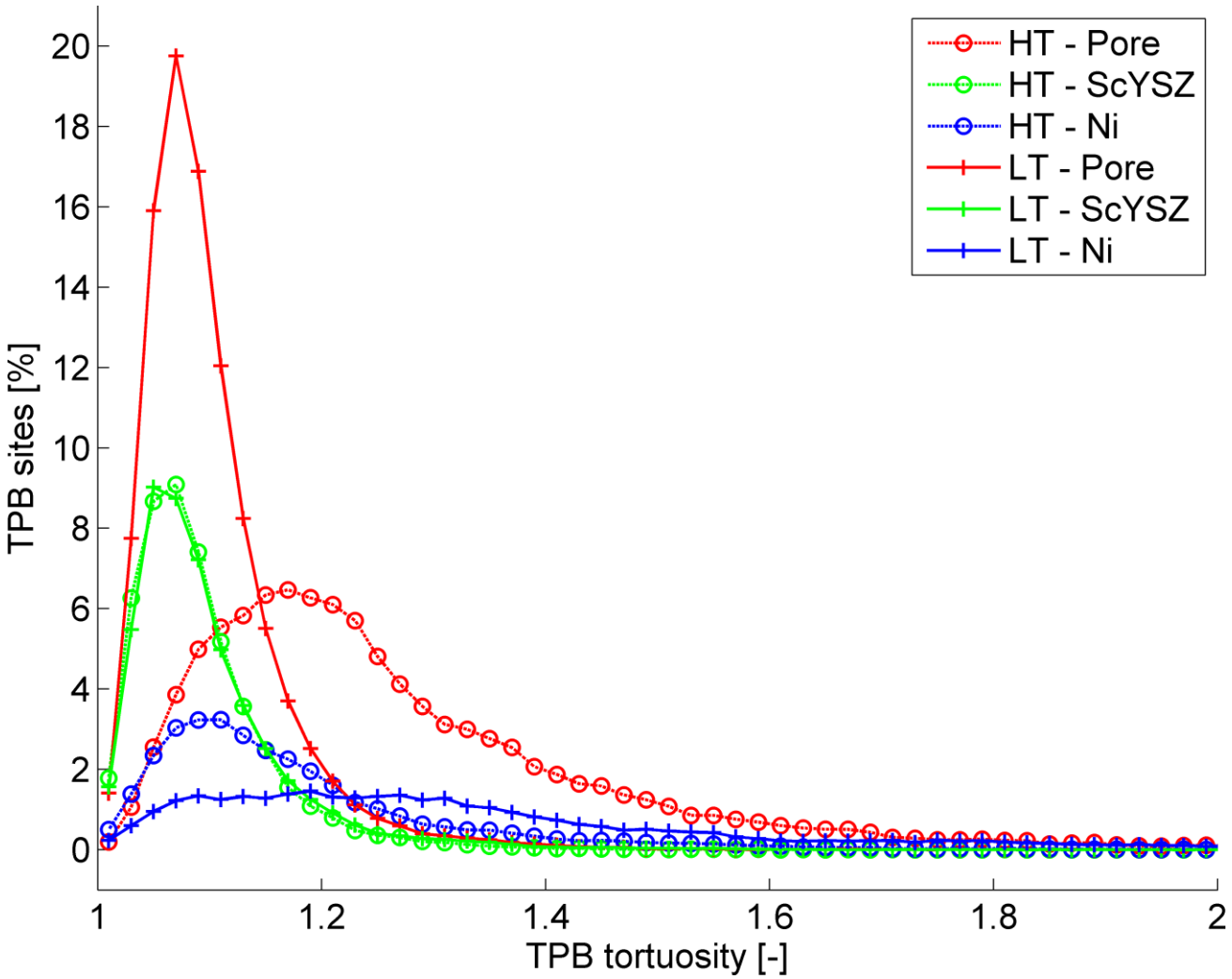

Figure 5: TPB tortuosity for all three phases for the LT-cell and HT-cell. Each curve represents the average from analysis of all 6 directions and only includes TPB sites further than 2.8 µm away from the source of the calculation.

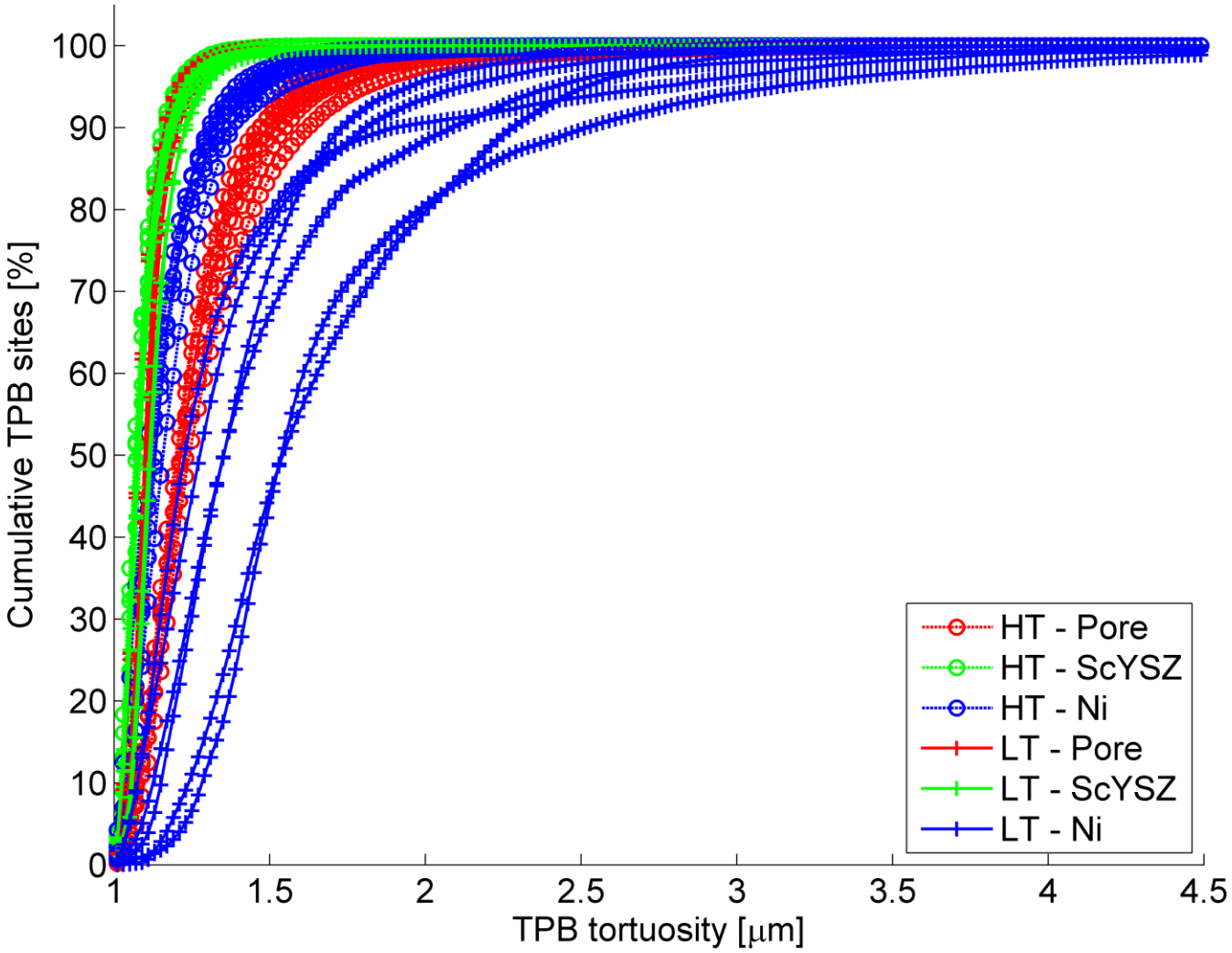

Figure 6: Cumulative TPB tortuosity for all three phases in the HT-cell and LT-cell. The graph shows all 6 directions for each of the two cells and for all three phases.

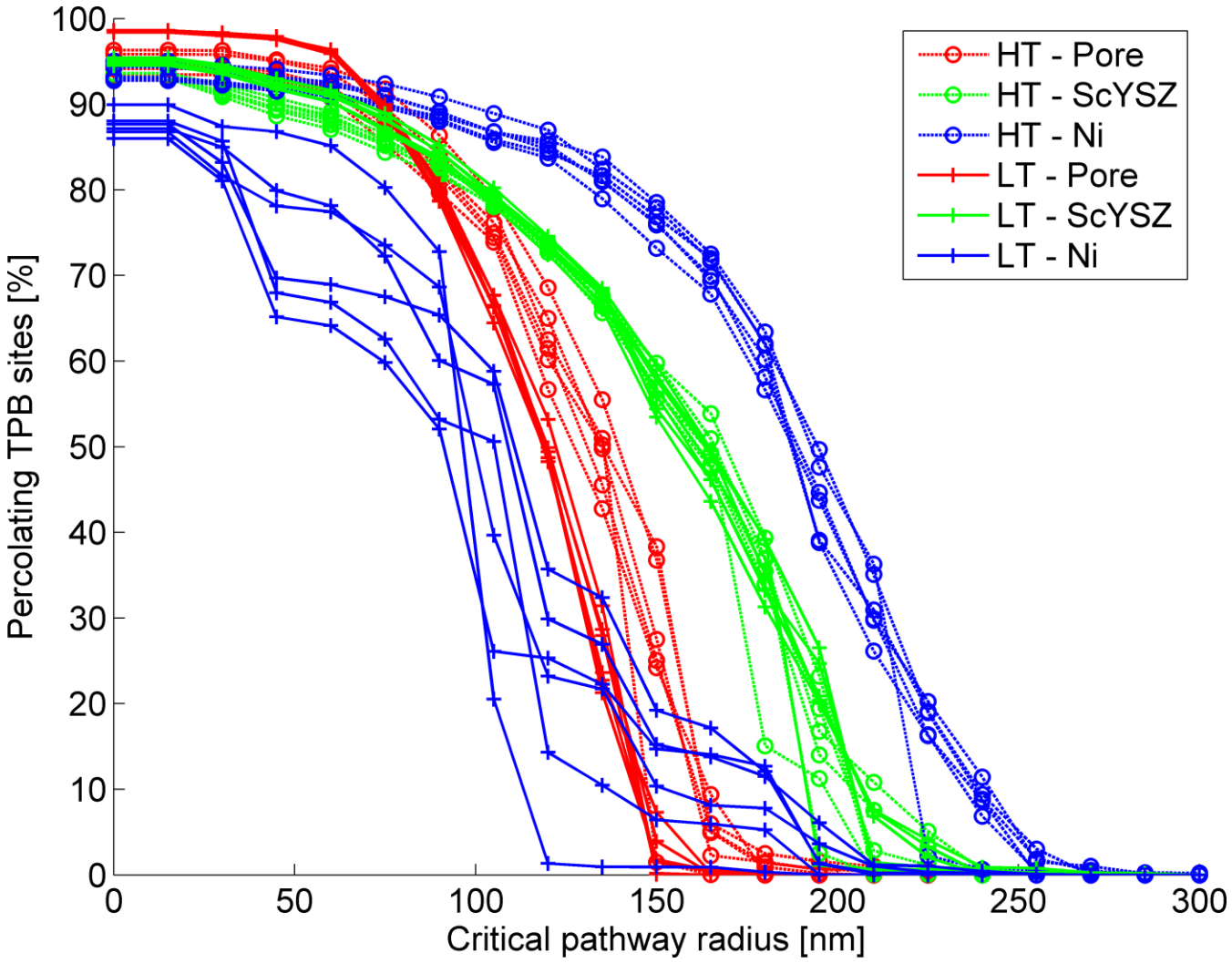

Figure 7: The critical pathway radius for all 3 phases for both cells and for all 6 directions.